more steeply with increasing radius, with the best-fit power law index becoming $\alpha = 2.5$. Correcting for clumping therefore seems to offer a simple solution to all the potential puzzles posed, at first glance, by the observed thermodynamic profiles of the Perseus Cluster at large radii. No additional physics is required by the data.

Our study shows no evidence for the puzzling deficit of baryons at $r \geq 0.5\ r_{200}$ inferred from some previous studies of other systems, using lower-quality data and/or extrapolated models (*26*–*30*). This suggests that within $r < 0.5\ r_{200}$ the physics of the x-ray–emitting gas is relatively simple, and x-ray measurements can be used robustly for cosmological work. At larger radii, however, the cluster gas is significantly clumped.

Numerical simulations predict gas clumping in the cluster outskirts (*31*). However, the amount of clumping depends on a large number of physical processes in the ICM which are currently uncertain; for example, viscosity, conduction, star formation feedback, and magnetic fields. Although our results were obtained for just one galaxy cluster, it is expected that the observed physical processes are common. Our results therefore provide an anchor for numerical models of ICM physics and for simulations of the formation and ongoing growth of galaxy clusters. An independent measurement of gas clumping can be obtained from the combination of x-ray and SZ observations, which have different dependences on the electron density.

References and Notes

1. S. D. M. White, J. F. Navarro, A. E. Evrard, C. S. Frenk, *Nature* **366**, 429 (1993).
2. A. Vikhlinin *et al.*, *Astrophys. J.* **692**, 1060 (2009).
3. A. Mantz, S. W. Allen, D. Rapetti, H. Ebeling, *Mon. Not. R. Astron. Soc.* **406**, 1759 (2010).
4. S. W. Allen, R. W. Schmidt, H. Ebeling, A. C. Fabian, L. van Speybroeck, *Mon. Not. R. Astron. Soc.* **353**, 457 (2004).
5. S. W. Allen *et al.*, *Mon. Not. R. Astron. Soc.* **383**, 879 (2008).
6. T. H. Reiprich *et al.*, *Astron. Astrophys.* **501**, 899 (2009).
7. M. R. George, A. C. Fabian, J. S. Sanders, A. J. Young, H. R. Russell, *Mon. Not. R. Astron. Soc.* **395**, 657 (2009).
8. M. W. Bautz *et al.*, *Pub. Astron. Soc. Jpn.* **61**, 1117 (2009).
9. A. Hoshino *et al.*, *Pub. Astron. Soc. Jpn.* **62**, 371 (2010).
10. M. Kawaharada *et al.*, *Astrophys. J.* **714**, 423 (2010).
11. K. Sato *et al.*, *Pub. Astron. Soc. Jpn.* **62**, 1423 (2010).
12. U. Feldman, *Phys. Scr.* **46**, 202 (1992).
13. J. S. Sanders, A. C. Fabian, *Mon. Not. R. Astron. Soc.* **381**, 1381 (2007).
14. M. Markevitch, A. Vikhlinin, *Phys. Rep.* **443**, 1 (2007).
15. Y. Fujita *et al.*, *Pub. Astron. Soc. Jpn.* **60**, 343 (2008).
16. S. Ettori, A. C. Fabian, D. A. White, *Mon. Not. R. Astron. Soc.* **300**, 837 (1998).
17. P. Tozzi, C. Norman, *Astrophys. J.* **546**, 63 (2001).
18. G. M. Voit, S. T. Kay, G. L. Bryan, *Mon. Not. R. Astron. Soc.* **364**, 909 (2005).
19. M. Arnaud *et al.*, *Astron. Astrophys.* **517**, A92 (2010).
20. J. F. Navarro, C. S. Frenk, S. D. M. White, *ApJ* **490**, 493 (1997).
21. S. J. LaRoque *et al.*, *Astrophys. J.* **652**, 917 (2006).
22. E. Komatsu *et al.*, *Astrophys. J. Suppl. Ser.* **192**, 18 (2011).
23. Y.-T. Lin, J. J. Mohr, *Astrophys. J.* **617**, 879 (2004).
24. A. H. Gonzalez, D. Zaritsky, A. I. Zabludoff, *Astrophys. J.* **666**, 147 (2007).
25. O. E. Young, P. A. Thomas, C. J. Short, F. Pearce, http://arxiv.org/abs/1007.0887 (2010).
26. S. Ettori, *Mon. Not. R. Astron. Soc.* **344**, L13 (2003).
27. I. G. McCarthy, R. G. Bower, M. L. Balogh, *Mon. Not. R. Astron. Soc.* **377**, 1457 (2007).
28. N. Afshordi, Y.-T. Lin, D. Nagai, A. J. R. Sanderson, *Mon. Not. R. Astron. Soc.* **378**, 293 (2007).
29. A. Vikhlinin *et al.*, *Astrophys. J.* **640**, 691 (2006).
30. S. Andreon, *Mon. Not. R. Astron. Soc.* **407**, 263 (2010).
31. M. Roncarelli *et al.*, *Mon. Not. R. Astron. Soc.* **373**, 1339 (2006).

32. We thank P. Thomas and O. Young for kindly providing the simulation results shown in Fig. 4. Support for this work was provided by NASA through Einstein Postdoctoral Fellowship grants number PF9-00070 and PF8-90056 awarded by the Chandra X-ray Center, which is operated by the Smithsonian Astrophysical Observatory for NASA under contract NAS8-03060. We acknowledge NASA grants NNX09AV64G and NNX10AR48G, issued through the Suzaku Guest Observer program, and grant NNX08AZ88G. The authors thank the Suzaku operation team and Guest Observer Facility, supported by JAXA and NASA. This work was supported in part by the U.S. Department of Energy under contract number DE-AC02-76SF00515. We also acknowledge the Grant-in-Aid for Scientific Research of the Ministry of Education, Culture, Sports, Science, and Technology of Japan (KAKENHI no. 22111513) and Chandra award GO0-11138B.

Supporting Online Material

www.sciencemag.org/cgi/content/full/331/6024/1576/DC1
SOM Text
References

11 November 2010; accepted 8 February 2011
10.1126/science.1200331

From a Single-Band Metal to a High-Temperature Superconductor via Two Thermal Phase Transitions

Rui-Hua He,[1,2,3]* M. Hashimoto,[1,2,3]* H. Karapetyan,[1,2] J. D. Koralek,[3,4] J. P. Hinton,[3,4] J. P. Testaud,[1,2,3] V. Nathan,[1,2] Y. Yoshida,[5] Hong Yao,[1,3,4] K. Tanaka,[1,2,3,6] W. Meevasana,[1,2,7] R. G. Moore,[1,2] D. H. Lu,[1,2] S.-K. Mo,[3] M. Ishikado,[8] H. Eisaki,[5] Z. Hussain,[3] T. P. Devereaux,[1,2]† S. A. Kivelson,[1]† J. Orenstein,[3,4]† A. Kapitulnik,[1,2]† Z.-X. Shen[1,2]†

The nature of the pseudogap phase of cuprate high-temperature superconductors is a major unsolved problem in condensed matter physics. We studied the commencement of the pseudogap state at temperature T^* using three different techniques (angle-resolved photoemission spectroscopy, polar Kerr effect, and time-resolved reflectivity) on the same optimally doped Bi2201 crystals. We observed the coincident, abrupt onset at T^* of a particle-hole asymmetric antinodal gap in the electronic spectrum, a Kerr rotation in the reflected light polarization, and a change in the ultrafast relaxational dynamics, consistent with a phase transition. Upon further cooling, spectroscopic signatures of superconductivity begin to grow close to the superconducting transition temperature (T_c), entangled in an energy-momentum–dependent manner with the preexisting pseudogap features, ushering in a ground state with coexisting orders.

As complex oxides, cuprate superconductors belong to a class of materials that exhibit many broken-symmetry states; unraveling the relationship between superconductivity in the cuprates and other possible broken-symmetry states has been a major challenge of condensed matter physics. A possibly related issue concerns the nature of the pseudogap in the cuprates and its relationship with superconductivity. Angle-resolved photoemission spectroscopy (ARPES) studies have shown that the pseudogap develops below a temperature T^* near the Brillouin zone boundary while preserving a gapless Fermi arc near the zone diagonal (*1*). A key issue is the extent to which the pseudogap is a consequence of superconducting fluctuations (*2*–*5*), which should exhibit a rough particle-hole symmetry, or another form of (incipient) order (*6*–*12*), which typically should induce particle-hole asymmetric spectral changes. Candidate orders include various forms of density wave, nematic, or unconventional magnetic orders that break different combinations of lattice translational (*6*–*8*, *13*–*19*), rotational (*6*, *9*, *15*, *17*, *20*–*22*), and time-reversal (*7*, *9*, *23*–*26*) symmetries.

We have focused on crystals of nearly optimally doped (OP) $Pb_{0.55}Bi_{1.5}Sr_{1.6}La_{0.4}CuO_{6+\delta}$ (Pb-Bi2201, $T_c = 38$ K, $T^* = 132 \pm 8$ K) (*27*), and combined the ARPES measurement of the evolution of the band structure over a wide range of

[1]Geballe Laboratory for Advanced Materials, Departments of Physics and Applied Physics, Stanford University, Stanford, CA 94305, USA. [2]Stanford Institute for Materials and Energy Sciences, SLAC National Accelerator Laboratory, Menlo Park, CA 94025, USA. [3]Advanced Light Source and Materials Sciences Division, Lawrence Berkeley National Laboratory, Berkeley, CA 94720, USA. [4]Department of Physics, University of California, Berkeley, CA 94720, USA. [5]Nanoelectronics Research Institute, National Institute of Advanced Industrial Science and Technology, Ibaraki 305-8568, Japan. [6]Department of Physics, Osaka University, Toyonaka, Osaka 560-0043, Japan. [7]School of Physics, Suranaree University of Technology and Synchrotron Light Research Institute, Nakhon Ratchasima, 30000 Thailand. [8]Japan Atomic Energy Agency, Tokai, Ibaraki 319-1195, Japan.

*These authors contributed equally to this work.
†To whom correspondence should be addressed. E-mail: zxshen@stanford.edu; aharonk@stanford.edu; jworenstein@lbl.gov; kivelson@stanford.edu; tpd@stanford.edu

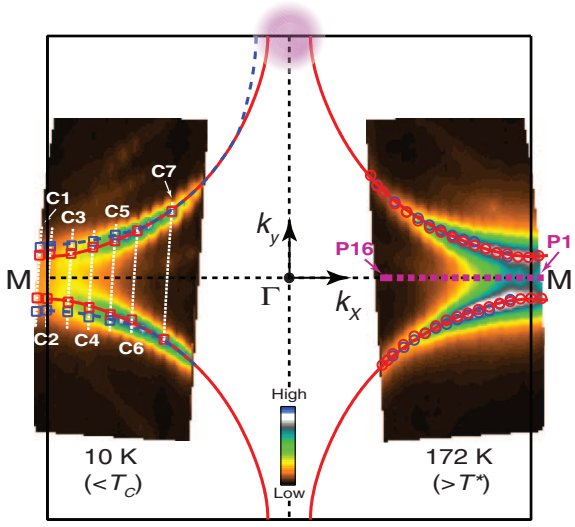

Fig. 1. Fermi surface maps measured below T_c at 10 K (**left**) and above T^* at 172 K (**right**) in the same momentum-space region (flipped for display). Dashed white lines labeled C1 to C7 depict the cuts along which the EDCs shown in Fig. 2, A to N, were measured. Magenta squares labeled P1 to P16 along M-Γ indicate momenta where EDCs in Fig. 2, V and W, were measured. Red and blue squares on the left indicate momenta of the Fermi-level crossing k_F (k_{F1} and k_{F2} in Fig. 2, A to G) at 172 K and back-bending k_G (black arrows in Fig. 2, O to S) at 10 K of the dispersion of the EDC maximum along cuts C1 to C7. Red and blue circles on the right indicate momenta of identifiable peaks in the momentum distribution curves (measured along cuts parallel to cut C7) at E_F at 172 K and 10 K, respectively. The solid red curves are a guide to the eye for the red squares and circles, whereas the dashed blue curve is the guide for the blue squares; together they show an increased k_G–k_F misalignment going away from the nodal toward the antinodal region. The magenta-shaded region is approximately where multiple EDC features are found at 10 K.

temperature, momentum, and energy, with high-precision measurements of the polar Kerr effect (PKE) and time-resolved reflectivity (TRR). Bi2201 was chosen to avoid the complications resulting from bilayer splitting and strong antinodal bosonic mode coupling inherent to $Bi_2Sr_2CaCu_2O_{8+\delta}$ (Bi2212) (*1*). Whereas ARPES is a surface probe, PKE enables us to monitor a bulk, thermodynamic (via the fluctuation-dissipation theorem) property that has proven (*28*) to be a sensitive probe of the onset of a broken-symmetry state, and TRR gives complementary information on the bulk, near-equilibrium dynamics of the system.

We will first analyze our ARPES data collected in different temperature regions. Above T^*, Pb-Bi2201 has a simple one-band band structure (right side of Fig. 1). For each cut in momentum space perpendicular to Γ-M [(0,0)-(π,0)] (C1 to C7 in Fig. 1), the only distinct feature in the corresponding Fermi-function–divided (*27*) energy distribution curves (EDCs) is a maximum (red circles in Fig. 2, A to G). As a function of the y component of the wave vector (k_y), the maxima have an approximately parabolic dispersion for

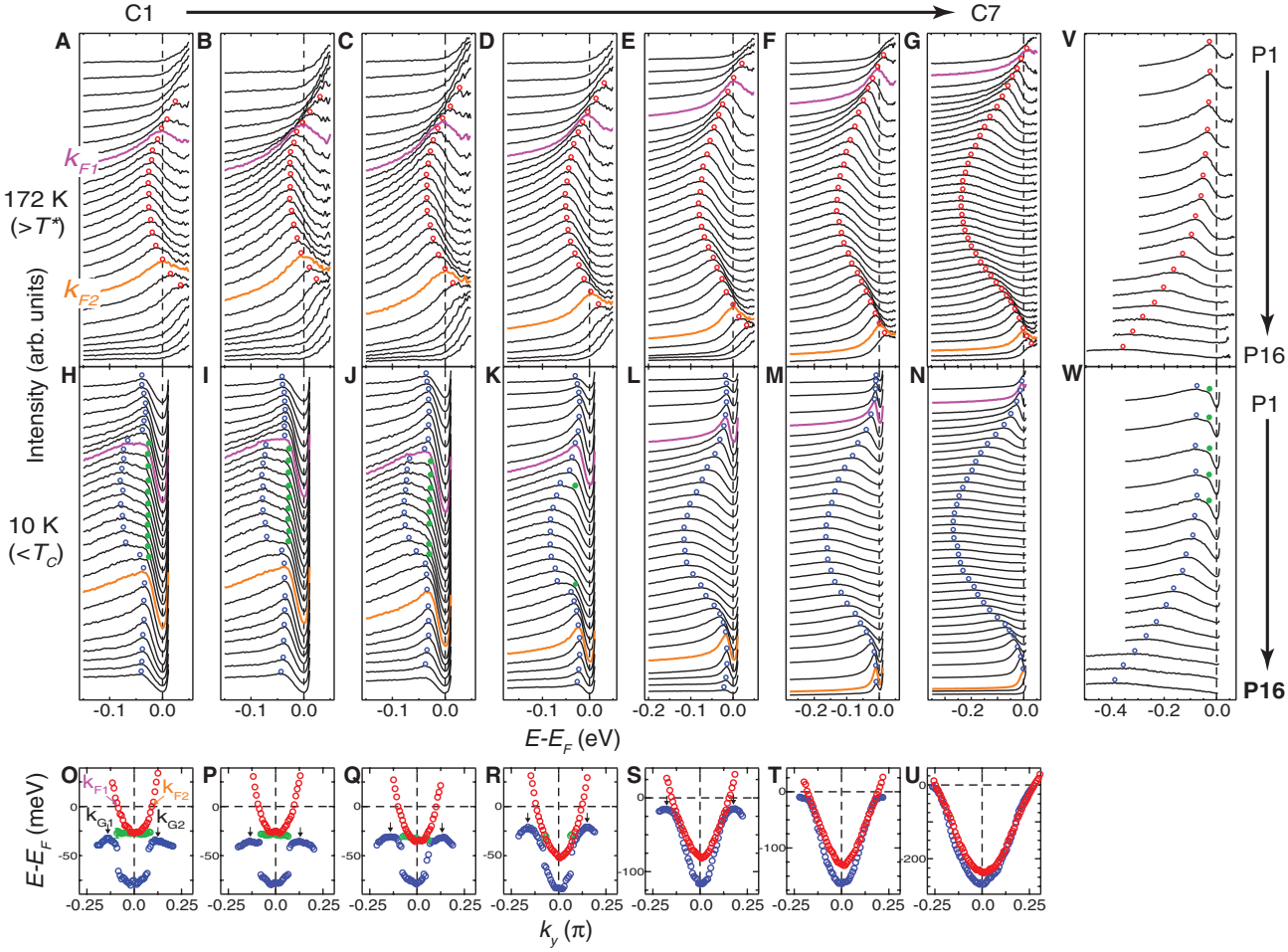

Fig. 2. (**A** to **G**) and (**H** to **N**) Selected EDCs at 172 K and at 10 K, respectively, for cuts C1 to C7, nearly perpendicular to Γ-M (Fig. 1). Each EDC corresponds to a white point in the cuts in Fig. 1. EDCs in magenta and orange are located close to k_F. (**O** to **U**) Dispersions of the EDC features in (A) to (N) for cuts C1 to C7. For each dispersion curve, every other symbol corresponds to an EDC in (A) to (N). Error bars are estimated based on the sharpness of features, to be ±3 meV minimum and ±8 meV maximum [examples shown in (O)] based on different EDC analyses (*27*). (**V** and **W**) EDCs at momenta P1 to P16 along M-Γ (Fig. 1) at 172 K and 10 K, respectively. Circles denote the EDC shoulder feature (solid green) and the EDC maximum feature at 10 K (blue) and at 172 K (red).

each cut (red circles in Fig. 2, O to U); the band bottom lies on the Γ-M axis, and the dispersion crosses the Fermi level (E_F) at two momenta, k_F (k_{F1} and k_{F2}). The binding energy of the band bottom monotonically decreases from near Γ to M (Fig. 2, O to U). We take the Fermi-level crossings of this single band to define the Fermi surface. Despite the simplicity of the electronic structure above T^*, the width and energy-dependent broadening of the EDC maximum features, along with the familiar strange metal behavior seen in transport, imply that the system is not well described as a Fermi liquid.

We now turn to the temperature region below T_c. Here, the entire Fermi surface is gapped except at the nodal points (k_F lying on the zone diagonal). In the nodal region, consistent with previous reports (*4*, *5*, *11*, *12*), a *d*-wave–like gap along the Fermi surface is observed that we quantify as the energy position of the EDC maximum (blue circles) at k_F (Fig. 2, L to N). This maximum is still the only identifiable feature in the EDC. By comparing the EDCs in Fig. 2, E to G, with those in Fig. 2, L to N, we see that the peaks of EDCs near k_F are much sharper below T_c than above T^*; however (perhaps surprisingly), the peaks well away from k_F appear broader but with larger experimental uncertainties (also see Fig. 2, V and W).

Away from the nodal region, the dispersion along each cut rises to a minimum binding energy and then bends back (Fig. 2, H to K). These back-bendings (black arrows in Fig. 2, O to S) occur at momenta k_G (k_{G1} and k_{G2}), which are increasingly separated from the Fermi surface (compare blue and red squares on the left side of Fig. 1) toward the antinodes (k_F lying on the zone boundary). Note that, for a superconducting gap, as a consequence of the particle-hole symmetry, one would expect $k_G \cong k_F$ (fig. S6), as is the case

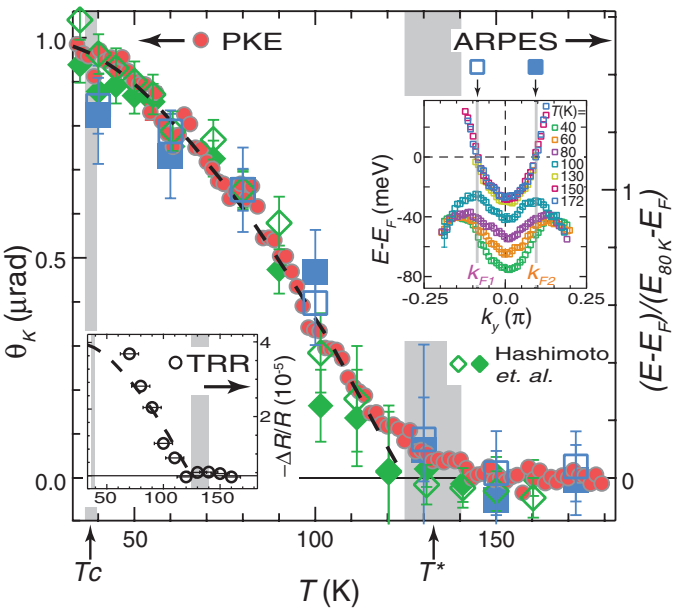

Fig. 3. Temperature dependence of Kerr rotation (θ_K) measured by PKE, in comparison with that of the binding energy position of the EDC maximum at k_F given by ARPES [reproduced from fig. S1F and (*29*)]. ARPES results are normalized to the 80 K values (free from the interference of fluctuating superconductivity). The dashed black curve is a guide to the eye for the PKE data, showing a mean-field–like critical behavior close to T^* [see additional discussion in (*27*)]. (**Left inset**) Temperature dependence of the transient reflectivity change measured by TRR (right axis). The dashed black curve (left axis) is reproduced from the main panel. Error bars (if not visible) are smaller than the symbol size. (**Right inset**) Dispersion of the EDC maximum at various temperatures above T_c, summarizing the results of Figs. 2A and 4A and fig. S1, A to E. All data were taken on samples from the same growth and annealing batch, except those reproduced from (*29*) on differently annealed samples.

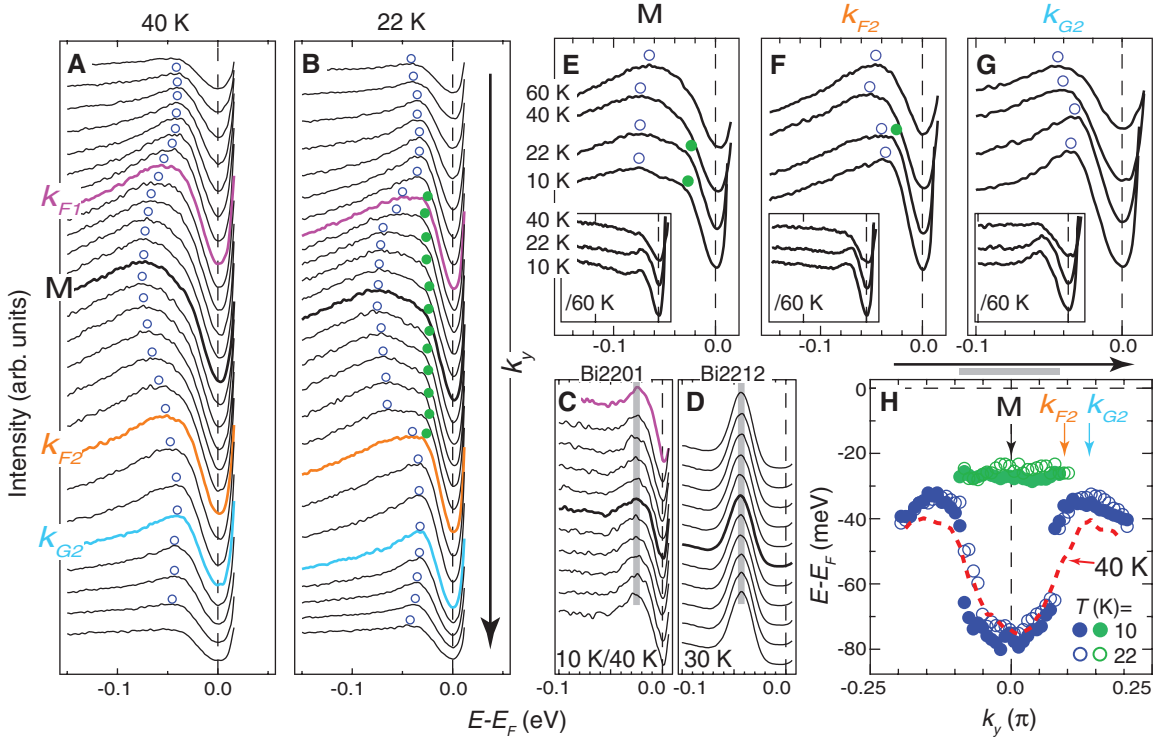

Fig. 4. (**A** and **B**) Selected EDCs at 40 K and 22 K along cut C1 (Fig. 1). See Fig. 2, A and H, for data at 172 K and 10 K, and fig. S1, A to E, for other intermediate temperatures. (**C**) Antinodal EDCs at 10 K after dividing by the 40 K counterparts, covering the momentum range indicated by the gray bar in (H), in comparison with those in (**D**) taken in a similar range at 30 K on an OP Bi2212 sample. Nondispersive peaks are seen in both cases despite different sharpness and energy positions. (**E** to **G**) EDCs at different fixed momenta [specified in (A) and (H)] and temperatures around T_c. The counterintuitive increase of the antinodal gap, defined by the energy position of the EDC maximum in (F) and (G), with temperature rising above T_c, cannot be understood with a single energy scale assumed. (Insets) Corresponding EDCs divided by the 60 K counterpart, showing the peaks losing definition above T_c (fig. S2E). (**H**) Summary for the dispersions of related EDC features across and below T_c. Vertical arrows specify momenta M, k_{F2} at 172 K, and k_{G2} at 10 K. Apparent asymmetry of the dispersions across M is due to a finite deviation of the cut from the high-symmetry direction and a subtle balance of spectral weight between different features in the EDC. All EDC features and error bars are similarly determined as in Fig. 2.

in the nodal region. The substantial k_G–k_F misalignment, previously found in a single antinodal cut perpendicular to Γ-M, has been interpreted as a signature of non–particle-hole symmetric order (*29*). Our observation here complements that finding by providing an entire momentum-space picture.

The width and shape of the EDC near k_F change fairly abruptly as a function of position along the Fermi surface, in contrast with the smooth evolution seen above *T** (compare magenta curves in Fig. 2, H to N and A to G). Strikingly, the antinodal EDC maxima below T_c are broader than those above *T** (Fig. 2, V and W, and fig. S7I). Such broadening of the antinodal spectra with decreasing temperature, as reported previously (*29*), is likely intrinsic, as the expected sharpening is observed simultaneously in the nodal spectra at low energy.

Around the M point, both the EDC line shape and the dispersion of the EDC maxima are more complex than their counterparts above *T**. The dispersion of the EDC maxima has two separate branches, one at relatively low energy, which shows back-bendings at k_G, and the other at higher energy around the band bottom on the Γ-M axis. As one moves from cuts C1 to C7, the apparent discontinuity between the two branches near the antinode vanishes and the two branches merge (Fig. 2, O to U). Both k_G (blue squares in Fig. 1) and the band-bottom energy (blue circles in Fig. 2W) evolve smoothly, even as the dispersion at intermediate energies changes dramatically.

Along with the changes in the dispersion of the EDC maxima below T_c, a well-defined shoulder feature (green dots in Fig. 2, H to K and W) (*27*) emerges at low energy in the EDCs. This feature exhibits little dispersion either along Γ-M (Fig. 2W) or perpendicular to it (Fig. 2, H to J). Unlike the EDC maxima, its dispersion does not continue toward the zone center (Fig. 2W) but instead loses its definition away from the vicinity of the M point (magenta-shaded region in Fig. 1).

The changes in the spectral function on cooling do not occur smoothly; instead, abrupt changes in the thermal evolution occur in the neighborhoods of *T** and T_c.

A detailed temperature-dependent study of an antinodal cut (C1 in Fig. 1) shows that the dispersion of the EDC maxima (blue circles in fig. S1, A to E) exhibit a transformation that begins at a temperature equal (within experimental uncertainty) to the reported values of *T** in the literature (*27*). Specifically, the energies of the EDC maxima at the band bottom and at k_F are temperature independent above *T** but begin shifting to higher binding energies below *T** (fig. S1F). The energy position at k_F is a measure of the pseudogap and can be defined as a spectral order parameter that becomes nonzero below *T**. Moreover, at temperatures below *T** but well above T_c, one can already see the k_G–k_F misalignment developing (right inset of Fig. 3). These observations are consistent with our previous report on a similar cut in an OP Pb-Bi2201 sample prepared under a different post-annealing condition (*29*).

It would be natural (as discussed below) to associate the abrupt change in nature of the ARPES spectra with a transition to a broken-symmetry state below *T**. To test this idea, we performed PKE measurements on the same crystals with finely spaced temperature steps (*27*). The results (Fig. 3) are clearly suggestive of a slightly rounded phase transition at *T** below which a finite Kerr rotation emerges. A similar transition in the Kerr rotation was previously observed in $YBa_2Cu_3O_{6+x}$ (YBCO) and was suggested to be linked to a broken-symmetry state that is not necessarily magnetic in nature (*25*). The smallness of the Kerr rotation in YBCO suggested that it might not reflect the primary order. The present data again show a small Kerr rotation; however, the strong correspondence between the ARPES and PKE data in Fig. 3 allows us to conjecture a phase transition at *T** and also to corroborate the interpretation of previously published data on YBCO in terms of a similar transition.

We also studied TRR on the same Pb-Bi2201 crystals (*27*). At temperatures between *Tc* and *T**, we observed a negative signal with a time-resolution–limited turn-on followed by decay on the order of 100 femtoseconds (fig. S3). Additionally, we observed a positive signal that emerges below T_c and decays on a picosecond time scale. These observations are consistent with previous studies of various cuprate families that revealed different dynamics above and below T_c (*30*), and associated the former with the pseudogap state (*31*–*36*). The striking aspects of the TRR results reported here are the clarity of the onset at T* and the direct correspondence with ARPES and PKE. As shown in the left inset of Fig. 3, the magnitude of the negative TRR signal tracks the ARPES and PKE data quite well. This added correspondence further supports the existence of a phase transition at T* to the pseudogap state with near-equilibrium dynamics distinct from superconductivity.

Upon cooling below T_c, it is observed in ARPES that the shoulder on the low-energy side of the EDC maximum appears to develop somewhat above T_c but well below *T**, and it grows truly distinct only below T_c (compare Fig. 4, A and B, with fig. S1, A to E). To obtain a clearer view of the structure of this feature, we show, in the insets of Fig. 4, E to G, the spectra at low temperatures divided by the one at 60 K—a procedure that converts the shoulder into a small peak. In Fig. 4C, we adopt the same procedure, but dividing by the 40 K spectra instead, and in fig. S2 we have subtracted off an approximate background from the EDCs. All three methods of analysis produce qualitatively similar results, with a small peak at a position that does not disperse appreciably along the exemplary antinodal cut C1. In all cases, the energy and width of the peak do not change considerably with increasing temperature, whereas the peak intensity is strongly temperature dependent; the peak becomes undetectable at a temperature that, although greater than T_c, is nowhere near *T**. This behavior of the processed data is highly reminiscent of the behavior of the superconducting coherence peak in Bi2212 (*37*), although that peak is visible in the raw data (Fig. 4D).

The strong and analogous temperature dependences of the ARPES, PKE, and TRR data seen between T_c and *T** are most naturally understood if *T** is associated with a phase transition to a nonsuperconducting broken-symmetry state (*27*). Although superconducting fluctuations are observable above T_c (Fig. 4, E to G, and fig. S2E), they appear to peter out at too low temperatures (being negligible already at 60 K) to play a central role in this higher-temperature transition. To complete this picture, it is necessary to identify the nature of the broken-symmetry state and to relate it to the apparently similar electronic changes that occur below *T** in other cuprates (*27*).

Below T_c, the nodal arc is gapped with a *d*-wave–like structure suggestive of a dominantly superconducting origin (*38*). In contrast, in the antinodal region, rather than one order being dominant, or the two gaps of both orders adding in quadrature, the spectral function develops a complex structure with two energy scales below E_F of mixed origin, a larger one being primarily associated with the pseudogap order and a smaller one with the superconducting order.

To see what can be learned about the pseudogap order from ARPES, we have used a simple mean-field model (*27*) to compute the expected changes to the band structure induced by various forms of density wave (*6*–*8*, *13*–*19*) (fig. S7) or nematic order (*6*, *15*, *17*, *20*–*22*) (fig. S8) coexisting with *d*-wave superconductivity. We note that some (but certainly not all) key aspects of our experimental observations can be qualitatively reproduced, regardless of which of these orders is assumed (*27*). An essential feature of both the experiment and the fits is the comparable sizes of the superconducting gap and the pseudogap. This implies that the two orders may have a more intimate connection than just competing orders, such as seen in 2*H*-$NbSe_2$, where the charge density wave gap is at least three times the superconducting gap (*39*).

References and Notes

1. A. Damascelli, Z. Hussain, Z.-X. Shen, *Rev. Mod. Phys.* **75**, 473 (2003).
2. V. J. Emery, S. A. Kivelson, *Nature* **374**, 434 (1995).
3. Y. Wang, L. Li, N. P. Ong, *Phys. Rev. B* **73**, 024510 (2006).
4. K. Nakayama *et al.*, *Phys. Rev. Lett.* **102**, 227006 (2009).
5. J. Meng *et al.*, *Phys. Rev. B* **79**, 024514 (2009).
6. S. A. Kivelson, E. Fradkin, V. J. Emery, *Nature* **393**, 550 (1998).
7. S. Chakravarty, R. B. Laughlin, D. K. Morr, C. Nayak, *Phys. Rev. B* **63**, 094503 (2001).
8. M. Grilli, G. Seibold, A. Di Ciolo, J. Lorenzana, *Phys. Rev. B* **79**, 125111 (2009).
9. C. M. Varma, *Phys. Rev. B* **55**, 14554 (1997).
10. K. Tanaka *et al.*, *Science* **314**, 1910 (2006).
11. T. Kondo *et al.*, *Nat. Phys.* **7**, 21 (2011).
12. J.-H. Ma *et al.*, *Phys. Rev. Lett.* **101**, 207002 (2008).
13. J. M. Tranquada, B. J. Sternlieb, J. D. Axe, Y. Nakamura, S. Uchida, *Nature* **375**, 561 (1995).

14. J. E. Hoffman *et al.*, *Science* **295**, 466 (2002).
15. C. Howald, H. Eisaki, N. Kaneko, A. Kapitulnik, *Proc. Natl. Acad. Sci. U.S.A.* **100**, 9705 (2003).
16. M. Vershinin *et al.*, *Science* **303**, 1995 (2004).
17. Y. Kohsaka *et al.*, *Science* **315**, 1380 (2007).
18. C. V. Parker *et al.*, *Nature* **468**, 677 (2010).
19. W. D. Wise *et al.*, *Nat. Phys.* **4**, 696 (2008).
20. V. Hinkov *et al.*, *Science* **319**, 597 (2008).
21. R. Daou *et al.*, *Nature* **463**, 519 (2010).
22. M. J. Lawler *et al.*, *Nature* **466**, 347 (2010).
23. A. Kaminski *et al.*, *Nature* **416**, 610 (2002).
24. B. Fauqué *et al.*, *Phys. Rev. Lett.* **96**, 197001 (2006).
25. J. Xia *et al.*, *Phys. Rev. Lett.* **100**, 127002 (2008).
26. Y. Li *et al.*, *Nature* **455**, 372 (2008).
27. Materials and methods are available as supporting material on *Science* Online.
28. J. Xia, Y. Maeno, P. T. Beyersdorf, M. M. Fejer, A. Kapitulnik, *Phys. Rev. Lett.* **97**, 167002 (2006).
29. M. Hashimoto *et al.*, *Nat. Phys.* **6**, 414 (2010).
30. G. L. Eesley *et al.*, *Phys. Rev. Lett.* **65**, 3445 (1990).
31. P. Gay *et al.*, *J. Low Temp. Phys.* **117**, 1025 (1999).
32. J. Demsar *et al.*, *Phys. Rev. Lett.* **82**, 4918 (1999).
33. R. A. Kaindl *et al.*, *Science* **287**, 470 (2000).
34. N. Gedik *et al.*, *Phys. Rev. B* **70**, 014504 (2004).
35. E. E. M. Chia *et al.*, *Phys. Rev. Lett.* **99**, 147008 (2007).
36. Y. H. Liu *et al.*, *Phys. Rev. Lett.* **101**, 137003 (2008).
37. A. V. Fedorov *et al.*, *Phys. Rev. Lett.* **82**, 2179 (1999).
38. That this is a bulk superconducting effect is corroborated by the magnetic field-dependent suppression of the Knight shift (a measure of the density of states at E_F) seen below T_c of Bi2201 in nuclear magnetic resonance (*40*). The Knight shift was found to drop sharply at T^*, exhibiting a similar temperature dependence as those shown in Fig. 3.
39. S. V. Borisenko *et al.*, *Phys. Rev. Lett.* **102**, 166402 (2009).
40. S. Kawasaki, C. Lin, P. L. Kuhns, A. P. Reyes, G. Q. Zheng, *Phys. Rev. Lett.* **105**, 137002 (2010).

41. We thank I. Vishik, W.-S. Lee, L. Taillefer, and M. Greven for helpful discussions, Y. Li and G. Yu for experimental assistance on SQUID, and J.-H. Chu on resistivity measurements. R.-H.H. thanks the SGF for financial support. This work at the Stanford Institute for Materials and Energy Sciences, the Stanford Synchrotron Radiation Lightsource, and the Advanced Light Source is supported by the Department of Energy, Office of Basic Energy Sciences under contracts DE-AC02-76SF00515 and DE-AC02-05CH11231.

Supporting Online Material

www.sciencemag.org/cgi/content/full/331/6024/1579/DC1
Materials and Methods
SOM Text
Figs. S1 to S8
References

28 September 2010; accepted 15 February 2011
10.1126/science.1198415

The Bonding Electron Density in Aluminum

Philip N. H. Nakashima,[1,2,3]* Andrew E. Smith,[1,4] Joanne Etheridge,[2,3] Barrington C. Muddle[1,2]

Aluminum is considered to approach an "ideal" metal or free electron gas. The valence electrons move freely, as if unaffected by the presence of the metal ions. Therefore, the electron redistribution due to chemical bonding is subtle and has proven extremely difficult to determine. Experimental measurements and ab initio calculations have yielded substantially different results. We applied quantitative convergent-beam electron diffraction to aluminum to provide an experimental determination of the bonding electron distribution. Calculation of the electron distribution based on density functional theory is shown to be in close agreement. Our results yield an accurate quantitative correlation between the anisotropic elastic properties of aluminum and the bonding electron and electrostatic potential distributions.

The electronic structure associated with chemical bonding affects all properties of materials except radioactivity. In metals, the widely taught concept of an ideal metal or free electron gas is popularly expressed as a regular array of metal ions surrounded by a sea of delocalized valence electrons (*1*). Although a gross simplification, this model is often sufficient to give a qualitative account of many characteristic properties of metals such as their high electrical and thermal conductivities and lustrous or shiny appearance (*1*–*3*). However, it fails to explain the often strong variation in particular properties of different metals that are sensitive to electronic structure (*2*–*4*)—for example, the anisotropy of elastic constants. One of the best examples of a free electron gas is aluminum (*2*, *5*).

Aluminum accounts for more than 40% of world production in nonferrous metals (*6*). The large global effort invested in refining aluminum and its alloys to extend property profiles involves the need for a fundamental understanding of metallic structure in solid solutions and structural evolution at the nanoscale in multiphase alloys. Such an effort must begin with accurate knowledge of the electronic structure, chemical bonding, and atomic-scale mechanics in pure aluminum (*2*–*4*, *7*–*12*), and then ultimately extend to its alloys (*2*, *8*, *9*, *13*).

A difficulty arising from aluminum's close approximation to a free electron gas is that the perturbation of the total electron distribution by chemical bonds is subtle and difficult to determine. As a consequence, extensive experimental and theoretical studies of the electron density in aluminum have been carried out since the 1920s (*7*, *8*, *14*–*17*) but have failed to reach a consensus on the electronic structure of the chemical bonds. All possible modes are represented in the literature, including bridge bonding between nearest neighbors (*17*), octahedrally centered bonding between second nearest neighbors (*7*, *17*), tetrahedrally centered bonding between nearest neighbors (*8*, *17*), and mixtures of these modes (*17*).

Using quantitative convergent-beam electron diffraction (QCBED), we have made absolute measurements of electronic structure at ambient and liquid helium–cooled temperatures that are of sufficient accuracy, precision, and resolution to establish the bonding electron distribution in aluminum unequivocally. Electron diffraction is intrinsically sensitive to electron distribution by virtue of the strong interaction of the electron with the electrostatic potential of the specimen. Using Wien2K (*18*), we performed an ab initio density functional theory (DFT) calculation of the electron distribution [using the generalized gradient approximation (GGA) in the full potential linearly augmented plane wave formalism (FPLAPW), incorporating local orbital and local screening potentials (lo + ls)] and found that it agrees closely with the experimental determination by QCBED. The bonding electron and potential distributions determined here have a strong quantitative correlation with the anisotropy of Young's modulus for aluminum.

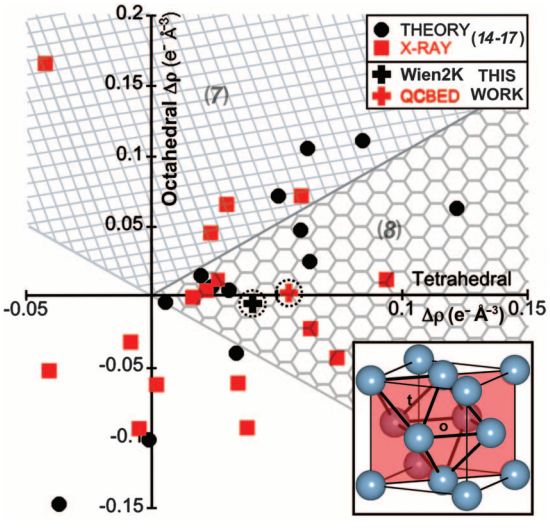

Fig. 1. Sets of F_g published since 1929 (*14*–*17*) are plotted as points on the graph of $\Delta\rho_{oct}$ at the octahedral site versus $\Delta\rho_{tet}$ at the tetrahedral site (o and t, respectively, in the inset). The DFT calculations of (*7*) would lie in the cross-hatched region of $\Delta\rho_{oct} > \Delta\rho_{tet}$. The full potential linear muffin tin orbital (FPLMTO) calculations of (*8*) would lie in the hexagon-hatched region of $\Delta\rho_{tet} > \Delta\rho_{oct}$. The present QCBED and Wien2K DFT (GGA/FPLAPW +lo +ls) (*18*) results are shown as circled crosses. See fig. S1 (*17*) for references for all points. All $\Delta\rho$ values were computed using the Eden Crystallography package (*29*).

[1]ARC Centre of Excellence for Design in Light Metals, Monash University, Victoria 3800, Australia. [2]Department of Materials Engineering, Monash University, Victoria 3800, Australia. [3]Monash Centre for Electron Microscopy, Monash University, Victoria 3800, Australia. [4]School of Physics, Monash University, Victoria 3800, Australia.

*To whom correspondence should be addressed. E-mail: philip.nakashima@eng.monash.edu.au